RSC Advances

PAPER

View Article Online
View Journal | View Issue

Cite this: *RSC Adv.*, 2023, **13**, 2339

Effect of calcium doping on the electrocatalytic activity of the $Bi_{1-x}Ca_xFeO_{3-\delta}$ oxygen electrode for solid oxide fuel cells†

Liang Wang, Tian Xia,* Liping Sun, Qiang Li* and Hui Zhao

Received 25th October 2022
Accepted 9th January 2023

DOI: 10.1039/d2ra06750a

rsc.li/rsc-advances

For solid oxide fuel cell (SOFC) applications, there remains a growing interest in developing efficient cathode catalysts. Herein, iron-based Ca-doped $Bi_{1-x}Ca_xFeO_{3-\delta}$ (BCF*x*, $x = 0.1$, 0.2, and 0.3) oxides are evaluated as potential cathode materials for SOFCs. The phase structure, thermal expansion behavior, electrical conductivity, and electrocatalytic properties for the oxygen reduction reaction (ORR) of the BCF*x* cathodes are systematically characterized. Among all compositions, the $Bi_{0.8}Ca_{0.2}FeO_{3-\delta}$ (BCF0.2) cathode exhibits the highest oxygen vacancy concentration and considerable electrocatalytic activity, demonstrating the lowest polarization resistance (0.11 Ω cm^2) and largest exchange current density of 41.91 mA cm^{-2} at 700 °C. The BCF0.2 cathode-based single cell delivers excellent output performance, yielding a maximum power density of 760 mW cm^{-2} 700 °C along with exceptional stability over a period of 60 h. This work highlights the Ca-doping strategy for enhancing electrocatalytic activity of the cathode electrocatalysts in SOFCs.

1. Introduction

Developing desirable cathode materials with outstanding electrocatalytic activity is a challenge for practical application in solid oxide fuel cells (SOFCs).[1,2] Among these materials, the Fe-based cathodes have attracted much attention due to their low cost, outstanding thermo-chemical stability, and acceptable electrocatalytic activity.[3–5]

In recent years, some efforts have been devoted to bismuth ferrite oxide ($BiFeO_3$, BFO) with low thermal expansion coefficient and excellent chemical compatibility, giving rise to efficient utilizations for the ORR and oxygen evolution reaction (OER).[6–8] Nevertheless, a secondary phase appears in BFO at 447–767 °C, which limits its practical applications.[9] Thus, improving thermodynamic stability is considered to be crucial to the BFO catalyst. The cation doping seems to be an effective strategy for stabilizing the phase structure of BFO.[10,11] Baek *et al.* reported that the Sr^{2+} doping significantly enhances oxygen surface exchange rate and thermal stability in $Bi_{1-x}Sr_xFeO_{3-\delta}$ (BSF).[12] The BSF materials are proposed to be potential cathodes for SOFCs because of their excellent electrocatalytic activity.[13] However, the electrical conductivity of BSF is not adequate (~1–2 S cm^{-1} in the temperature range of 300 and 900 °C). Recently, it is found that partial substitution of Ca^{2+} for Bi^{3+} can promote the chemical compatibility and electrocatalytic performance.[14] Moreover, the Ca doping also enhanced the electrical conductivity of BFO.[15] Increased oxygen vacancy concentration in the bulk may be responsible for improved structural stability.[16] In this scheme, we believe that $Bi_{1-x}Ca_xFeO_{3-\delta}$ should be promising cathode materials for SOFCs.

In this work, a series of $Bi_{1-x}Ca_xFeO_{3-\delta}$ (BCF*x*, $x = 0.1$, 0.2, and 0.3) oxides are synthesized and evaluated as potential Fe-based cathode electrocatalysts for SOFCs. The crystal structure, surface states, and thermal expansion behavior are systematically characterized. The electrochemical properties and electrode reaction kinetics for ORR are discussed in detail. Furthermore, the BCF*x* cathode-based fuel cell shows satisfactory SOFCs performance.

2. Experimental section

2.1 Materials preparation

$Bi_{1-x}Ca_xFeO_{3-\delta}$ (BCF*x*, $x = 0.1$, 0.2, and 0.3) oxides were synthesized by a sol–gel method. Stoichiometric amounts of $Bi(NO_3)_3 \cdot 3H_2O$, $Ca(NO_3)_2 \cdot 4H_2O$, and $Fe(NO_3)_3 \cdot 9H_2O$ were mixed and dissolved into deionized water to form a transparent solution, with additions of citric acid and EDTA (citric acid : EDTA : total metal ion = 2 : 1 : 1 in molar ratio). The above solution was heated at 100 °C to produce the viscous gel. Afterwards, this gel was heated at 180 °C for 6 h, and then calcined at 850 °C for 12 h to obtain the final products.

2.2 Material characterization

The phase composition of BCF*x* powders was analyzed using an X-ray diffractometer (XRD, Bruker AXS D8 Advance) with a Cu-

Key Laboratory of Functional Inorganic Material Chemistry, Ministry of Education, School of Chemistry and Materials Science, Heilongjiang University, Harbin 150080, P. R. China. E-mail: xiatian@hlju.edu.cn; liqiang@hlju.edu.cn

† Electronic supplementary information (ESI) available. See DOI: https://doi.org/10.1039/d2ra06750a

Kα radiation ($\lambda = 1.5418$ Å) source in the 2θ range of 20–80°. The microstructure of the cells was observed using scanning electron microscopy (SEM) (Supra 55 Sapphire Carl ZEISS). The conductivity of BCF*x* was measured using standard four-probe method with a Keithley 2700 digital multimeter. The BCF*x* powders were pressed at a pressure of 230 MPa and then sintered at 900 °C for 12 h to obtain the rectangular bars (12 × 2 × 1.5 mm). Thermal expansion coefficients (TECs) of BCF*x* were recorded with a dilatometer (SETARAMM Setsys 18) within a temperature range of 50–800. X-ray photoelectron spectra (XPS) were conducted on a Kratos Axis Ultra DLD instrument with a radiation source of Al Kα (1486.6 eV). Electron paramagnetic resonance (EPR) spectra were performed with Bruker EPR100d X-band spectrometer. Thermogravimetric (TG) tests were performed using TG/DTA 6300 thermal analyzer (PerkinElmer, USA) in air atmosphere in temperature range of 50–800 °C. The oxygen non-stoichiometry value (δ) of samples at elevated temperatures was calculated by thermogravimetric analysis (TGA) and iodometric titration data.

2.3 Electrochemical characterization

The dense $Ce_{0.9}Gd_{0.1}O_{1.9}$ (GDC) electrolyte (thickness: ~350 mm, diameter: ~15 mm) was fabricated by pressing GDC powder (Ningbo SuoFuRen Energy Co. Ltd) and then sintered at 1400 °C for 24 h. To fabricate symmetric cells with the BCF*x*|GDC|BCF*x* configuration, the cathode ink was prepared by thoroughly mixing BCF*x* powder and organic binder. The cathode ink was symmetrically printed on both sides of the GDC substrate and then calcined at 900 °C for 4 h to obtain symmetrical cells. Electrochemical impedance spectroscopy (EIS) was acquired on symmetric cells with an electrochemical workstation (Autolab PGSTAT302N) in the frequency range of 10^{-2}–10^{6} Hz at 500–700 °C. For CO_2 tolerance experiment, EIS of the cathode was tested at 700 °C in a mixture atmosphere with different CO_2 concentrations (1, 3, 5 and 10 vol.% in air). For preparing the three-electrode cells, the cathode ink is deposited onto one side of the GDC electrolyte as the working electrode. Silver paste was used as the counter electrode and was painted on the opposite side of GDC substrate. The silver reference electrode was placed on the same side of the working electrode. The anode-supported fuel cells (NiO-YSZ|(YSZ, $Zr_{0.84}Y_{0.16}O_2$)|GDC|BCF*x*) were fabricated for the fuel cell test. The half-cells of NiO-YSZ|YSZ|GDC were purchased from Ningbo SuoFuRen Energy Co. Ltd. The cathode ink was painted onto the GDC buffer layer and then calcined at 900 °C for 4 h. The single cell is sealed at the end of an alumina tube with high-temperature ceramic binder. The anode side is supplied with humidified H_2 (80 mL min^{-1}) and the cathode side is exposed to ambient air. Current–voltage (*I*–*V*) curves of the fuel cells were tested with an electrochemical workstation (IM6ex, ZAHNER) over a temperature range of 500–700 °C.

3. Results and discussion

Fig. 1a shows the XRD patterns of the BCF*x* powders after calcining at 850 °C for 12 h. The BCF*x* materials have a cubic

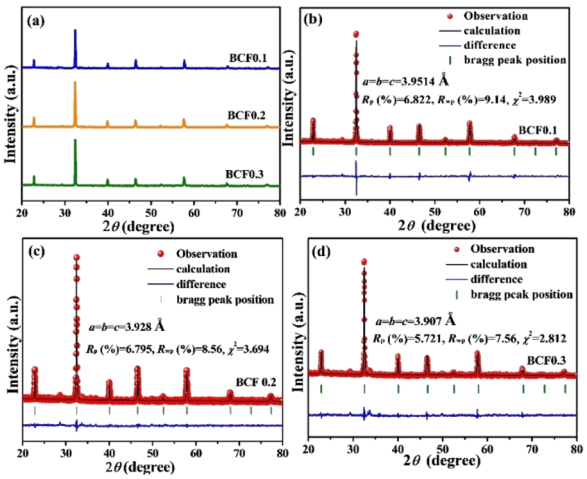

Fig. 1 (a) Room temperature XRD patterns of the BCF*x* powders. Rietveld refinement profiles of (b) BCF0.1, (c) BCF0.2, and (d) BCF0.3.

perovskite structure with space group $Pm\bar{3}m$, without any secondary phases. Furthermore, to understand detailed crystal structure of BCF*x*, the XRD patterns were refined using Rietveld refinement method (Fig. 1b–d). As can be seen clearly, the lattice parameters decrease gradually with increasing the Ca^{2+} concentration. This fact is mainly attributed to smaller ionic radius of Ca^{2+} (1 Å) than that of Bi^{3+} (1.04 Å), leading to the contraction of unit cell volume.[17] The acceptable reliable factors mean a rationality for structural refinements. Aiming at probing chemical compatibility between BCF*x* and GDC, the BCF*x*–GDC mixtures were calcined at 850 °C for 12 h. The relevant XRD patterns are shown in Fig. S1.† It is found that all diffraction peaks are assigned to both BCF*x* and GDC components. Not any visible impurities can be detected in the mixtures, indicating that BCF*x* has a good chemical compatibility with GDC electrolyte.

Fig. 2a shows the electrical conductivities of the BCF*x* samples over the temperature range of 100–800 °C in air. The electrical conductivity of all perovskites increases at elevated temperature, suggesting a semi-conducting nature arising from small polaron-type hopping.[18] The maximum conductivities are 6.43, 6.74, and 6.48 S cm^{-1} for BCF0.1, BCF0.2, and BCF0.3 at 800 °C, respectively. These values surpass that of undoped $BiFeO_3$ (1.32 S cm^{-1})[6] and are comparable to those of high-performance Fe-based cathode materials, such as $Bi_{0.5}Sr_{0.5}Fe_{0.9}Nb_{0.1}O_{3-\delta}$ (3.3 S cm^{-1}),[19] $BaFe_{0.95}Sn_{0.05}O_{3-\delta}$ (7.8 S cm^{-1}),[20] and $Bi_{0.5}Sr_{0.5}Fe_{0.95}Zr_{0.05}O_{3-\delta}$ (5.97 S cm^{-1}).[21]

Fig. 2b presents the thermal expansion curves of the BCF*x* samples in the temperature range of 50–800 °C. The average TEC value of BCF*x* increases with increasing the doping fraction. As usual, the TEC value is inversely proportional to the bonding energy of oxides.[22] It is noteworthy that the bonding energy of Bi–O is larger than that of Ca–O, thereby giving rise to increased TEC. The average TEC values are 12.8, 14.8, and 17.0 × 10^{-6} K^{-1} for BCF, BCF0.2, and BCF0.3, respectively. These TEC values here are much lower than those of some Fe-based cathodes[23–25] and are compatible with the GDC electrolyte

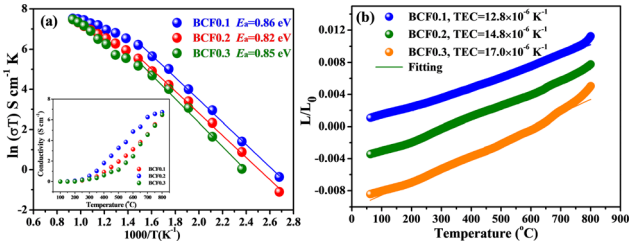

Fig. 2 (a) Arrhenius plots of electrical conductivity of BCF*x* in air. (b) Thermal expansion curves of BCF*x* in the temperature range of 50–800 °C.

(13.0×10^{-6} K^{-1}),[26] which benefits for the thermo-chemical stability between cathode and electrolyte.

Fig. 3a shows the O 1s XPS spectra of the BCF*x* materials. All O 1s spectra consist of two peaks. The peaks at 531.3–531.6 eV correspond to surface adsorbed oxygen (O_{ads}), while the peaks at 528.4–528.9 eV are associated with the lattice oxygen (O_{lat}).[27] The percentages of O_{ads}/O_{lat} derived from the peak areas are summarized in Fig. 3b. Noticeably, the BCF0.2 sample has the largest O_{ads}/O_{lat} value (2.42), signifying that BCF0.2 possesses great surface oxygen adsorption properties.[28] Fig. 3c displays the Fe $2p_{3/2}$ spectra of the BCF*x* samples. According to the reports, three subpeaks centered at 711.7–712.1 eV, 710–710.9 eV, and 709.0–709.4 eV are related to Fe^{4+}, Fe^{3+}, and Fe^{2+}, respectively,[29,30] and the fitting results of are listed in Table S1.† The average valence states of Fe are +3.058, +3.119, and +3.233 for BCF0.1, BCF0.2, and BCF0.3, respectively. Meanwhile, the calculated oxygen non-stoichiometry (δ) values of BCF*x* are 0.021, 0.041, and 0.034 for BCF0.1, BCF0.2, and BCF0.3, respectively. Furthermore, EPR spectroscopy was used to probe the presence of oxygen vacancies in the BCF*x* samples, as presented in Fig. 3d. The main resonance line is located at a magnetic field strength of 321.14 G, which is consistent with typical EPR signal with the *g* value of 2.228.[31] This originates from the unpaired electrons trapped in oxygen vacancy species.

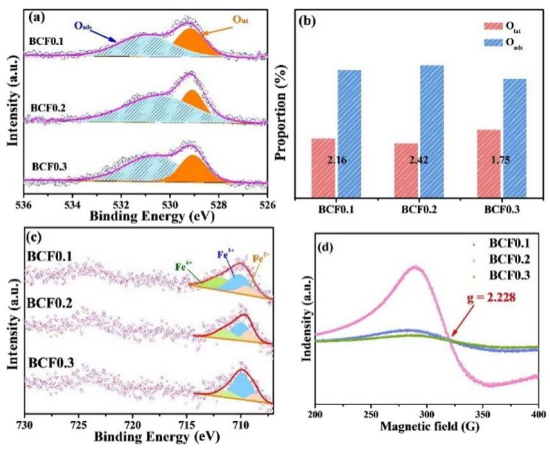

Fig. 3 (a) O 1s XPS spectra, (b) the percentages of O_{ads} and O_{lat}, and (c) Fe 2p XPS spectra of the BCF*x* samples. (d) EPR spectra of the BCF*x* samples.

Furthermore, the oxygen non-stoichiometry of BCF*x* materials at elevated temperatures was investigated by the TGA (Fig. S2a†). We can find that before 300 °C, the three materials show slow weight loss, mainly because the materials show adsorbed water vapor and hydrocarbons. With the further increase of temperature, the material begins to show obvious weight loss, mainly due to the loss of lattice oxygen in the material, which will also cause the change of Fe valence state and the formation of oxygen vacancies. The oxygen non-stoichiometry (δ) of the BCF*x* samples at elevated temperatures was explored by TGA in air, as presented in Fig. S2b.† The δ values were determined by TGA results and the initial oxygen non-stoichiometry (δ_0) values at room temperature were obtained by the iodometric titration. The BCF0.2 possesses the largest oxygen vacancy concentration, indicating its excellent oxygen ions mobility and promoted ORR activity.

The ORR activity of the BCF*x* electrodes with symmetric configuration (BCF*x*|GDC|BCF*x*) was evaluated by EIS. As shown in Fig. 4a, the R_P values of BCF0.1, BCF0.2, and BCF0.3 electrodes are 0.27, 0.11, and 0.62 Ω cm^2 at 700 °C, respectively. Among all cathodes, the BCF0.2 electrode gives the lowest R_P values at 600–700 °C (Fig. 4b), reflecting the best electrochemical performance of BCF0.2. This performance of BCF0.2 outperforms many cobalt-free electrodes (Fig. 4c).[32–36] Fig. 4d shows the Arrhenius plots of R_p for the BCF*x* cathodes. The activation energy (E_a) values of the BCF0.1, BCF0.2, and BCF0.3 cathodes are 124.4, 110.8, and 122.4 kJ mol^{-1}, respectively. The lowest E_a facilitates the oxygen mobility and electrocatalytic activity of BCF0.2 and is smaller than those of reported Fe-based cathodes, *e. g.* $La_{0.8}Ca_{0.2}Fe_{0.8}Ni_{0.2}O_{3-\delta}$ (178 kJ mol^{-1}),[32] $LaFe_{0.8}Cu_{0.2}O_{3-\delta}$ (159.2 kJ mol^{-1}),[37] $La_{0.5}Sr_{0.5}Fe_{0.9}Mo_{0.1}O_{3-\delta}$ (146.6 kJ mol^{-1}),[38] and $PrBaFe_2O_{5+\delta}$ (123.5 kJ mol^{-1}).[39]

The sintering temperature plays a key role in the electrode performance. Fig. 5a shows the EIS spectra of the BCF0.2 electrode calcined at different temperatures (850 °C, 900 °C, and

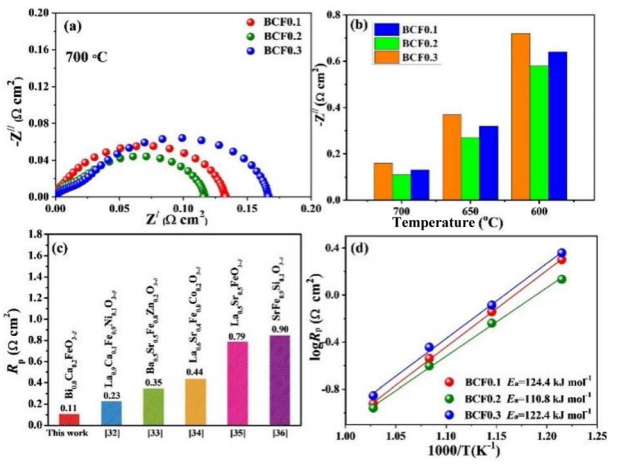

Fig. 4 (a) Nyquist plots of EIS spectra of the symmetrical cells with the BCF*x* electrodes at 700 °C. (b) Comparison of the R_p values for the BCF*x* cathodes at 600–700 °C. (c) Comparison of the R_p value of BCF0.2 with those of Fe-based cathodes at 700 °C. (d) Arrhenius plots of R_p for BCF*x* cathodes at 500–700 °C.

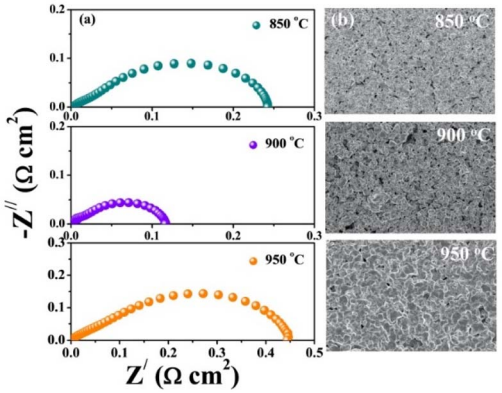

Fig. 5 (a) EIS spectra of the BCF0.2 cathode at different sintering temperatures and then measured at 600–700 °C. (b) SEM images of the BCF0.2 cathode calcined at different temperatures.

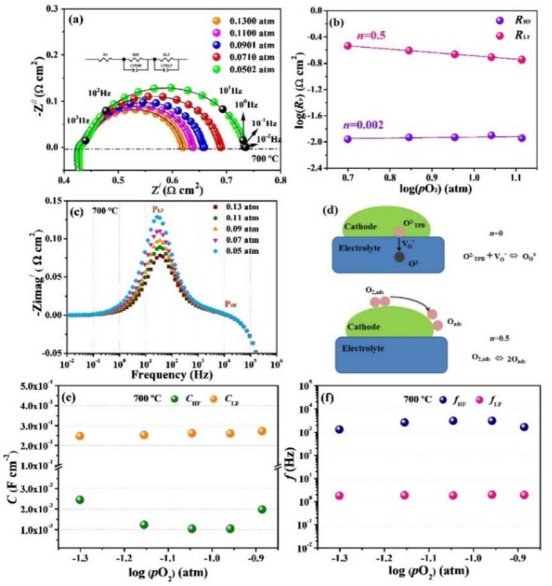

Fig. 6 (a) Nyquist plots of EIS spectra of the BCF0.2 cathode under various pO_2 at 700 °C. (b) RHF and RLF of the BCF0.2 cathode as a function of oxygen partial pressure at 700 °C. (c) Bode plots of the BCF0.2 cathode under various pO_2 at 700 °C. (d) Schematic illustration of ORR at the cathode/electrolyte interface; (e) C and (f) f values of the BCF0.2 cathode as a function of oxygen partial pressure at 700 °C.

950 °C). When sintering temperature is 900 °C, the R_P value reaches the lowest level measured at 700 °C, manifesting that appropriate calcining temperature may make the best electrochemical performance. Furthermore, the effect of calcining temperature on the electrode microstructure is also explored (Fig. 5b). At the lower calcining temperature (850 °C), the electrode layer shows poor connection between cathode particles. The surface-section view reveals a moderate porous structure with well-connected network after calcining at 900 °C. Such microstructure provides convenient gas diffusion and charge transfer, further improving electrocatalytic ORR activity of the electrode.[40] However, the cathode particles aggregate at higher treatment temperature (950 °C), resulting in decreased ORR kinetics and increased polarization resistance.[41] Thus, the electrode should be calcined at 900 °C to realize the best electrochemical performance toward ORR.

To go insight into the ORR mechanism, the EIS spectra of the BCF0.2 cathode were tested at different oxygen partial pressures (pO_2) at 700 °C (Fig. 6a). All impedance spectra consist of high-frequency and low-frequency arcs, indicating that two reaction steps occur for ORR at least. The impedance data was fitted using the equivalent circuit $R_1 - (R_{HF}/CPE_{HF}) - (R_{LF}/CPE_{LF})$, where R_1 is the ohmic resistance from the electrolyte and measuring device, R_{HF} and R_{LF} represent high-frequency and low-frequency resistance, and CPE_{HF} and CPE_{LF} are the constant phase elements. As we know, the relationship between R_P and pO_2 can be expressed by the following equation: $R_P = k(pO_2)^{-n}$ (1), where k is the independent constant, and the n values represent different ORR steps on the electrode.[42] The dependence of R_{HF} and R_{LF} for the BCF0.2 electrode on pO_2 at 700 °C is plotted in Fig. 6 (b). The n value is 0.07 in the high-frequency region, which is indicative of oxide-ion transport from three-phase boundary (TPB) to electrolyte ($n = 0$).[43] The characteristic n value related to the low-frequency region is 0.51, suggesting the oxygen adsorption/dissociation process on the catalyst surface ($n = 1/2$).[44] Bode plots of impedance spectra are further discussed, as shown in Fig. 6c. Bode curves can be involved into two peaks: high-frequency peak (P_{HF}) and low-frequency peak (P_{LF}). The peak area for P_{HF} presents a slight dependence on pO_2, while P_{LF} dramatically changes with pO_2. The results further confirms that the oxygen adsorption-dissociation process is the rate-limiting step for ORR, as schematically illustrated in Fig. 6d. In addition, the ORR steps at the BCF0.2 electrode interface was also clarified by calculating the characteristic capacitance (C) and relaxation frequency (f).[45] The C_{HF} and f_{HF} values in high-frequency range are 10^{-3}–10^{-2} F cm^{-2} and 10^3–10^4 Hz (Fig. 6e and f, and Table S2†), respectively, which is related to the charge transfer reaction.[46] For the low-frequency contribution, the C_{LF} and f_{LF} values are 0.2–0.3 F cm^{-2} and 10^{-1}–10^2 Hz, respectively, corresponding to oxygen adsorption/dissociation process.[47]

To further develop the bifunctional application of BCF0.2 in the ORR and OER manners, the polarization curves were tested with a three-electrode cell using chronoamperometry method. The overpotentials for both ORR and OER models decrease with increasing temperature, suggesting enhanced electrocatalytic activity at elevated temperature. For the ORR mode, the current density reaches −268 mA cm^{-2} at an overpotential of −55 mV. This current density value is larger than those of some cobalt-based cathodes at the same overpotential.[48,49] For the OER mode, the anodic overpotential is as low as 37.4 mV when the current density is 284 mA cm^{-2}. Furthermore, the important parameter, exchange current density (i_0), is used to evaluate the ORR activity. Tafel plots of the BCF0.2 cathode at 600–700 °C are shown in Fig. 7b. The i_0 can be calculated by the Boult Volmer equation: $\eta = RT\ln(i)/\alpha ZF - RT\ln(i_0)/\alpha ZF$ (2).[50] The corresponding i_0 values of BCF0.2 are 11.67, 31.42, and 41.91 mA cm^{-2} at 600, 650, and 700 °C, respectively. At 700 °C, the i_0 value is superior to those of some reported cobalt-free cathodes, such

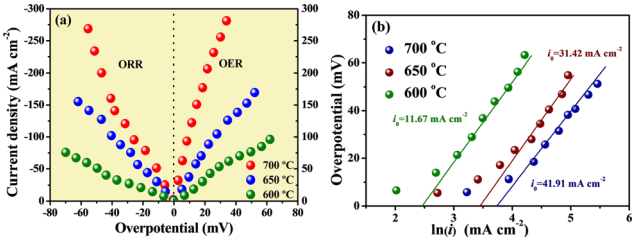

Fig. 7 (a) Polarization curves of the BCF0.2 electrode in the ORR and OER models at 600–700 °C. (b) Tafel plots of the BCF0.2 cathode at 600–700 °C.

as Pr_2CuO_4 (9.8 mA cm^{-2}),[51] $Ca_2Fe_{1.3}Mn_{0.7}O_{5+\delta}$ (18.2 mA cm^{-2}),[52] and $Pr_{0.8}Sr_{0.2}FeO_{3-\delta}$ (34.3 mA cm^{-2}).[53] Resultantly, the BCF0.2 catalyst is proposed to be utilized as promising bifunctional electrode.

To further investigate electrocatalytic activity of the cathode, an anode-supported single cell with the configuration of NiO-YSZ|YSZ|GDC|BCF*x* was fabricated. Fig. 8a–c show the *I–V* and *I–P* curves of single cells with the BCF*x* cathodes at 600–700 °C using humidified hydrogen (3% H_2O) and ambient air as the fuel and oxidant, respectively. The maximal power densities (MPD) of single cells are 634, 760, and 594 mW cm^{-2} for BCF0.1, BCF0.2 and BCF0.3 at 700 °C, respectively. The BCF0.2 cathode-based single cell delivers the best output performance, and the MPD value is higher than those of Fe-based cathode-containing fuel cells, such as $BaBi_{0.05}Co_{0.8}Nb_{0.15}O_{3-\delta}$ (218 mW cm^{-2}),[54] $Ba_{0.95}La_{0.05}Fe_{0.8}Zn_{0.2}O_{3-\delta}$ (266.5 mW cm^{-2}),[55] and $SrFe_{0.8}Sb_{0.2}O_{3-\delta}$ (450 mW cm^{-2}).[56] Moreover, the long-term stability was further tested at a constant voltage of 0.5 V at 700 °C. The single cell shows stable MPD and current density over a period of 60 h operation without negligible degradation rate (Fig. 8d), indicating exceptional operating stability of the fuel cell.

CO_2 tolerance is a prominent parameter to evaluate the possible application of the cathode. In general, alkaline earth-containing electrode oxide are always generated with CO_2 form a carbonate on the cathode surface, which are averse to the adsorption and diffusion of oxygen.[57] To assess the CO_2 tolerance of BCF0.2, the EIS spectra are measured at 700 °C in air with different CO_2 concentration. As shown the Fig. S3a,† it can be found that the polarization resistance values of BCF0.2 cathode increases with the CO_2 concentration. Obviously, the polarization resistance values of the electrode increased from 0.11 to 0.156 Ω cm^2 and 0.224 to 0.347 Ω cm^2 for BCF0.2 and $Bi_{0.5}Sr_{0.5}FeO_{3-\delta}$ (BSF) cathode (Fig. S3b†). Compared with BSF electrode, it can be found that the Ca doped electrode has better CO_2 tolerance than the Sr doped electrode.

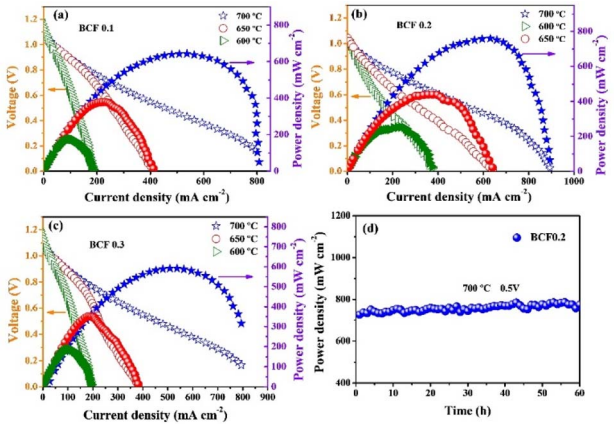

Fig. 8 (a–c) *I–V* and *I–P* curves of the NiO-YSZ|YSZ|GDC|BCF*x* single cells at 600–700 °C. (d) Long-term stability test of single cell with the BCF0.2 cathode at 700 °C.

4. Conclusions

In summary, the Fe-based BCF*x* oxides have been synthesized and evaluated as efficient cathode catalysts for SOFCs. The Ca^{2+} substitution promotes the amount of absorbed oxygen and enhances the cathode performance of BCF*x*. Among all components, the BCF0.2 cathode exhibits excellent ORR activity, as evidenced by the lowest R_p (0.11 Ω cm^2) and highest MPD (0.76 W cm^{-2}) at 700 °C. Furthermore, EIS analysis indicates that the oxygen adsorption/dissociation process is the main rate-limiting step toward ORR. Additionally, the BCF0.2 electrode yields a higher current density in both ORR and OER manners, demonstrating bifunctional characteristic of the BCF0.2 electrode. This study endows an effective way for designing novel cathode electrocatalysts in SOFCs.

Conflicts of interest

There are no conflicts to declare.

Acknowledgements

The project was supported by National Natural Science Foundation of China (51972100) and Natural Science Foundation of Heilongjiang Province (ZD2022E007).

References

1 Z. P. Shao and S. M. Haile, *Nature*, 2004, **431**, 170–173.
2 X. M. Xu, Y. L. Pan, Y. J. Zhong, R. Ran and Z. P. Shao, *Mater. Horiz.*, 2020, **7**, 2519–2565.
3 J. M. Porras-Vazquez, T. Pike, C. A. Hancock, J. F. Marco, F. J. Berry and P. R. Slater, *J. Mater. Chem. A*, 2013, **38**, 11834–11841.
4 J. T. Gao, Q. Li, W. W. Xia, L. P. Sun, L. H. Huo and H. Zhao, *ACS Sustainable Chem. Eng.*, 2019, **7**, 18647–18656.
5 T. Hong, M. Y. Zhao, K. Brinkman, F. L. Chen and C. G. Xia, *ACS Appl. Mater. Interfaces*, 2017, **9**, 8659–8668.
6 R. A. Afzal, K. Y. Park, S. H. Cho, N. I. Kim, S. R. Choi, J. H. Kim, H. T. Lim and J. I. Park, *RSC Adv.*, 2017, **7**, 47643–47653.
7 T. W. Chen, P. Kalimuthu, G. Anushya, S. M. Chen, R. Ramachandran, V. Mariyappan and D. C. Muthumala, *Materials*, 2021, **14**, 2976.
8 I. Papadas, J. A. Christodoulides, G. Kioseoglou and G. S. Armatas, *J. Mater. Chem. A*, 2015, **3**, 1587–1593.

9 S. M. Selbach, M. A. Einarsrud and T. Grande, *Chem. Mater.*, 2009, **21**, 169–173.
10 L. Li, Z. Q. Kong, B. W. Yao, H. Yang, Z. H. Gao, L. J. Xu, F. F. Dong, M. Ni and Z. Lin, *Chem. Eng. J.*, 2020, **396**, 125237.
11 P. Anand, D. P. Jaihindh, W. K. Chang and Y. P. Fu, *Appl. Surf. Sci.*, 2021, **540**, 148387.
12 D. Baek, A. Kamegawa and H. Takamura, *Solid State Ionics*, 2014, **262**, 691–695.
13 Y. J. Niu, J. Sunarso, W. Zhou, F. L. Liang, L. Ge, Z. H. Zhu and Z. P. Shao, *Int. J. Hydrogen Energy*, 2011, **36**, 3179–3186.
14 M. Schrade, N. Masó, A. Perejón, L. A. Pérez-Maqueda and A. R. West, *J. Mater. Chem. C*, 2017, **5**, 10077–10086.
15 N. Masó and A. R. West, *Chem. Mater.*, 2012, **24**, 2127–2132.
16 J. S. Lim, J. H. Lee, H. S. Park, R. Gao, T. Y. Koo, L. W. Martin, R. Ramesh and C. H. Yang, *NPG Asia Mater.*, 2018, **10**, 943–955.
17 F. Sánchez-De Jesús, A. M. Bolarín-Miró, C. A. Cortés-Escobedo, A. Barba-Pingarrón and F. Pedro-García, *J. Alloys Compd.*, 2020, **824**, 153944.
18 J. W. Stevenson, T. R. Armstrong, L. R. Pederson and W. J. Weber, *J. Electrochem. Soc.*, 1996, **143**, 2722–2729.
19 L. Gao, Q. Li, L. P. Sun, L. H. Huo, H. Zhao and J. C. Grenier, *J. Power Sources*, 2017, **371**, 86–95.
20 F. F. Dong, M. Ni, W. He, Y. B. Chen, G. M. Yang, D. J. Chen and Z. P. Shao, *J. Power Sources*, 2016, **326**, 459–465.
21 J. T. Gao, D. Ma, H. Zhao, Q. Li, Z. Lü and B. Wei, *Energy*, 2022, **252**, 124050.
22 A. R. Ruffa, *J. Mater. Sci.*, 1980, **15**, 2258–22567.
23 J. H. Zhang, F. Z. Han, C. X. Li and S. L. Zhang, *J. Eur. Ceram. Soc.*, 2022, **42**, 5801–5812.
24 Y. J. Wu, S. Wang, Y. Gao, X. Yu, H. T. Jiang, B. Wei and Z. Lü, *J. Alloys Compd.*, 2022, **926**, 166852.
25 X. Y. Lu, Y. Yang, Y. Z. Ding, Y. H. Chen, Q. W. Gu, D. Tian, W. L. Yu and B. Lin, *Electrochim. Acta*, 2017, **227**, 33–40.
26 H. Hayashi, M. Kanoh, C. J. Quan, H. Inaba, S. R. Wang, M. Dokiya and H. Tagawa, *Solid State Ionics*, 2000, **13**, 227–233.
27 L. Gao, Q. Li, L. P. Sun, L. H. Huo, H. Zhao and J. C. Grenier, *J. Mater. Chem. A*, 2018, **6**, 15221–15229.
28 J. W. Yin, Y. M. Yin, J. Lu, C. M. Zhang, N. Ming and Z. F. Ma, *J. Phys. Chem.*, 2014, **118**, 13357–13368.
29 C. C. Wang, M. Gholizadeh, B. X. Hou and X. C. Fan, *RSC Adv.*, 2021, **11**, 7–14.
30 T. Z. Ma, T. Xia, Q. Li, L. P. Sun, L. H. Huo and H. Zhao, *J. Eur. Ceram. Soc.*, 2022, **42**, 490–498.
31 C. Z. Sun, Y. Kong, L. Shao, K. N. Sun and N. Q. Zhang, *J. Power Sources*, 2020, **459**, 228017.
32 N. O. Vitoriano, C. B. López, A. Hauch, I. R. D. Larramendi and T. Rojo, *Int. J. Hydrogen Energy*, 2014, **39**, 6675–6679.
33 B. Wei, Z. Lu, X. Q. Huang, M. L. Liu, N. Li and W. H. Su, *J. Power Sources*, 2008, **176**, 1–8.
34 E. P. Murray, M. J. Sever and S. A. Barnett, *Solid State Ionics*, 2002, **148**, 27–34.
35 Y. J. Niu, J. Sunarso, F. L. Liang, W. Zhou, Z. H. Zhu and Z. P. Shao, *J. Electrochem. Soc.*, 2011, **158**, B132–B138.
36 J. M. Porras-Vazquez, T. Pike, C. A. Hancock, J. F. Marco, F. J. Berry and P. R. Slater, *J. Mater. Chem. A*, 2013, **1**, 11834–11841.
37 A. Idrees, X. N. Jiang, G. Liu, H. Luo, G. Q. Jia, Q. Y. Zhang, L. Jiang, X. N. Li and B. M. Xu, *ChemistryOpen*, 2018, **7**, 688–695.
38 M. Wu, H. Cai, F. Jin, N. Sun, J. Xu, L. Zhang, X. Han, S. Wang, X. Su, W. Long, L. Wang and L. Zhang, *J. Eur. Ceram. Soc.*, 2021, **41**, 2682–2690.
39 G. D. Li, Y. J. Gou, X. J. Cheng, Z. Bai, R. Z. Ren, C. M. Xu, J. S. Qiao, W. Sun, Z. H. Wang and K. N. Sun, *ACS Appl. Mater. Interfaces*, 2021, **13**, 34282–34291.
40 W. W. Xia, Q. Li, L. P. Sun, L. H. Huo and H. Zhao, *J. Alloys Compd.*, 2020, **835**, 1545406.
41 L. Gao, M. Z. Zhu, T. Xia, Q. Li, T. S. Li and H. Zhao, *Electrochim. Acta*, 2018, **289**, 428–436.
42 J. R. Wilson, D. T. Schwartz and S. B. Adler, *Electrochim. Acta*, 2006, **51**, 1389–1402.
43 Y. Takeda, R. Kanno, M. Noda, Y. Tomida and O. Yamamoto, *J. Electrochem. Soc.*, 1987, **134**, 2656–2661.
44 E. Siebert, A. Hammouche and M. Kleitz, *Electrochim. Acta*, 1995, **40**, 1741–1753.
45 M. J. Escudero, A. Aguadero, J. A. Alonso and L. Daza, *Electroanal. Chem.*, 2007, **611**, 107–116.
46 A. B. Yu, T. Xia, L. P. Sun, Q. Li, L. H. Huo and H. Zhao, *J. Alloys Compd.*, 2020, **837**, 155563.
47 X. N. Li, X. N. Jiang, S. L. Pang, Q. Wang, Z. X. Su and Q. Y. Zhang, *Int. J. Hydrogen Energy*, 2011, **36**, 13850–13857.
48 M. M. Guo, Q. Li, J. T. Gao, L. P. Sun, L. H. Huo and H. Zhao, *J. Alloys Compd.*, 2021, **858**, 158265.
49 F. C. Meng, T. Xia, J. P. Wang, Z. Shi and H. Zhao, *J. Power Sources*, 2015, **293**, 741–750.
50 B. C. H. Steele, *Solid State Ionics*, 1995, **75**, 157–165.
51 C. Sun, Q. Li, L. P. Sun, H. Zhao and L. H. Huo, *Mater. Res. Bull.*, 2014, **53**, 65–69.
52 Q. Li, L. P. Sun, X. Zeng, H. Zhao, L. H. Huo, J. C. Grenier, J. M. Bassat and F. Mauvy, *J. Power Sources*, 2013, **238**, 11–16.
53 J. H. Piao, K. N. Sun, N. Q. Zhang, X. B. Chen, S. Xu and D. R. Zhou, *J. Power Sources*, 2007, **172**, 633–640.
54 X. W. Meng, G. H. Long, S. X. Liu, Y. Ji, M. J. Pang, B. Wang, S. Q. Lü and J. H. Yang, *Int. J. Hydrogen Energy*, 2015, **40**, 6935–6941.
55 Z. Wang, P. F. Lv, L. Yang, R. Guan, J. D. Jiang, F. J. Jin and T. M. He, *Ceram. Int.*, 2020, **46**, 18216–18223.
56 Y. Q. Meng, L. Sun, J. Gao, W. Z. Tan, C. S. Chen, J. X. Yi, H. J. M. Bouwmeester, Z. H. Sun and K. S. Brinkman, *ACS Appl. Mater. Interfaces*, 2019, **11**, 11498–11506.
57 M. M. Guo, T. Xia, Q. Li, L. P. Sun and H. Zhao, *J. Eur. Ceram. Soc.*, 2021, **41**, 6531–6538.